De novo designed bifunctional proteins for targeted protein degradation

Bram Mylemans[1,2], Boguslawa Korona[3], Amanda M. Acevedo-Jake[4], Ailsa MacRae[4], Thomas A. Edwards[5], Danny T. Huang[6,7], Andrew J. Wilson[4,8,9]*, Laura S. Itzhaki[3]* and Derek N. Woolfson[1,2,10,11]*

[1]School of Chemistry, University of Bristol, Cantock's Close, Bristol BS8 1TS, UK

[2]Novo Nordisk Foundation Center for Protein Design, Department of Biology and Department of Drug Design and Pharmacology, University of Copenhagen, Jagtvej 160, 2100 Copenhagen, DK

[3]Department of Pharmacology, University of Cambridge, Cambridge CB2 1PD, UK

[4]School of Chemistry, University of Birmingham, Edgbaston, B15 2TT, UK

[5]College of Biomedical Sciences, Larkin University, 18301 N Miami Ave #1, Miami, Florida, 33169 USA

[6]Cancer Research UK Scotland Institute, Garscube Estate, Switchback Road, Glasgow G61 1BD, UK

[7]School of Cancer Sciences, University of Glasgow, Garscube Estate, Switchback Road, Glasgow G61 1QH, UK

[8]School of Chemistry, University of Leeds, Woodhouse Lane, Leeds LS2 9JT, UK

[9]Astbury Centre for Structural Molecular Biology, University of Leeds, Woodhouse Lane, Leeds LS2 9JT, UK

[10]School of Biochemistry, University of Bristol, Medical Sciences Building, University Walk, Bristol BS8 1TD, UK

[11]Max Planck-Bristol Centre for Minimal Biology, University of Bristol, Cantock's Close, Bristol BS8 1TS, UK

*To who correspondence should be addressed:
a.j.wilson.1@bham.ac.uk; Lsi10@cam.ac.uk; and D.N.Woolfson@bio.ku.dk

Author contributions: BM, BK, DH, AJW, LSI and DNW conceived the project and designed the experiments. BM designed the scaffold and binders, and purified and characterised them using solution-phase biophysics. AMAJ and AM purified the target proteins and measured the binding affinities of the binders against them. BM and AMAJ determined the protein X-ray crystal structures with help from TAE. BK performed all cell assays. BM and DNW wrote the paper. All authors have read and contributed to the preparation of the manuscript. TAE, LSI, DNW, and AJW raised the funding.

ABSTRACT

Targeted protein degradation (TPD) is a therapeutic strategy to remove disease-causing proteins by routing them to the ubiquitin-proteasome, autophagy, or lysosme machineries. For instance, proteolysis-targeting chimeras (PROTACs) are synthetic hetero-bifunctional small molecules that simultaneously bind the target and an E3 ubiquitin ligase to drive ubiquitination and degradation by the proteasome. Despite considerable success, designing such molecules is challenging and the number of currently addressable ubiquitin E3 ligases is limited. Here we demonstrate hetero-bifunctional *de novo* designed proteins as alternatives for TPD to access more targets and ligases. First, we develop a stable and highly adaptable helix-turn-helix scaffold for presenting different binding sites. Next, we use computational protein design to incorporate and embellish hot-spot- binding sites to target BCL-x_L, plus short linear motifs (SLiMs) for KLHL20 ligase recruitment. The resulting mono- and bi-functionalised proteins bind the targets *in vitro*, and the latter degrade BCL-x_L in cells leading to apoptosis.

MAIN

Over the past two decades, targeted protein degradation (TPD) has developed into a promising therapeutic strategy[1,2]. While multiple degradation machineries are under investigation[3,4], the proteasome remains the most extensively studied[1,2,5]. For instance, molecular glue degraders[6] and proteolysis-targeting chimeras (PROTACs)[7] simultaneously bind a protein of interest (POI) and an E3 ubiquitin ligase (E3), inducing ubiquitination of the POI and its subsequent proteasomal degradation. Unlike classical inhibitors, PROTACs can work by engaging any region of the POI and are not limited to recognition of functional sites. Through this encounter-driven mechanism, the process can be catalytic, with multiple copies of a POI being eliminated by each PROTAC molecule[1,2,8]. As a result, lower doses of cytotoxic compounds can be used[9].

Despite encouraging progress in clinical trials[5], bottlenecks remain for small-molecule PROTACs. The degradation efficiency is driven by ternary complex formation, which depends on multiple factors, including individual binding constants of the two recognition elements, linker lengths between them, the locations of binding sites on the targets and proximity of suitable lysine residues to which ubiquitin can be conjugated[8]. Secondly, despite the vast potential E3 repertoire, most PROTACs harness just two E3s – Cereblon (CRBN) or von Hippel-Lindau (VHL)[5,10,11]. Whilst this is changing with new E3 ligands being described[12-14],exploring new modes of targeting and binding the POI and ligases will help advance and generalise the technology[1]. For instance, peptide-based PROTACs[15] have the potential to overcome these limitations by using natural short linear motifs (SLiMs) as a common protein-protein interaction (PPI) modality to access more targets and E3s[7,16-18]. However, SLiMs often have weak binding affinities, making it difficult to direct precise and stable complex formation.

Recent advances in protein-structure prediction and protein design might help overcome these limitations. Deep learning-based methods have accelerated the fields dramatically[19-22], with AlphaFold2[23] and related methods[24] for rapid and accurate modelling, and tools such as RFdiffusion[25] and ProteinMPNN[26] for *de novo* protein backbone and sequence design, respectively. Computational design pipelines, either alone or in combination with experimental screening of many variants, are achieving protein binders approaching pM binding affinities[27-29]. In addition, tools like BindCraft[29] are democratizing binder design, and allow targeting of specific regions on the POI's surface. These successes have encouraged the field to move beyond binding a single protein. For example, proteins have been designed to inhibit multiple different POIs,[30] or to display multiple viral epitopes[31]. Designed proteins have been fused together via a flexible linker to drive internalisation of membrane proteins[32] or to cause degradation or stabilisation of intracellular targets[33]. Nonetheless, these strategies do not leverage the full potential of protein design, which, in principle, allows for the precise positioning of multiple binding sites to drive specific ternary complex formation.

101 Here, we describe a *de novo* designed protein-based PROTAC. For the POI, we target
102 BCL-x_L, a member of the therapeutically important B-cell lymphoma 2 (BCL-2) family. BCL-x_L
103 is an anti-apoptotic protein that can be inhibited by binding helical peptide effectors leading to
104 apoptosis[34,35]. As this interaction is well characterised with high-resolution X-ray crystal
105 structures[36], together with homologues such as MCL-1 it has served as a testing ground for
106 developing methods leading to the design of many peptide-, protein- and small-molecule-
107 based binders[37-40]. Moreover, due to interest in BCL-x_L as an anti-apoptotic cancer target,
108 small-molecule inhibitors and PROTACs have been developed for it[41]; *e.g.*, a PROTAC
109 synthetic molecule, DT2216, is currently undergoing clinical trials[42]. Like many PROTACs, this
110 uses a VHL-binding ligand to induce ubiquitination. Recently, we have identified other E3s
111 compatible with TPD of BCL-x_L, including Kelch-like protein 20 (KLHL20) with an in-cell, GFP-
112 based degradation assay (accompanying manuscript). X-ray crystal structures[43] indicate that
113 the KLHL20 binding-competent SLiM adopts a compact loop conformation. Indeed, binding
114 affinity can be improved by constraining the SLiM as a cyclic peptide, and these have been
115 used in the design of small-molecule/peptide hybrid PROTACs[17].
116 To generate and validate a *de novo* protein-based PROTAC against BCL-x_L, we
117 develop the following design pipeline (Fig. 1a). First, using rationally seeded computational
118 protein design[44], we make a straightforward helix-loop-helix scaffold. Next, we add a binding
119 site for BCL-x_L using hot-spot-grafting combined with ProteinMPNN optimisation and
120 AlphaFold2 modelling and evaluation. To test the versatility of the scaffold and approach, we
121 design and compare binders for BCL-x_L and MCL-1, exploring specificity with *in vitro* binding
122 assays and structural studies. Subsequently, we graft on a SLiM (degron) for KLHL20 and
123 optimise its binding affinity. These bindings sites were tested individually in the in-cell, GFP-
124 based degradation assay for their capacity to act as targeting sequences or degrons. Finally,
125 the best performing binding sequences were combined and assessed for their ability to
126 degrade BCL-x_L and induce apoptosis in a lung-cancer cell line. Specifically, we compare
127 single and bifunctional constructs with binding sites against BCL-x_L and/or KLHL20, and the
128 small molecule in clinical trials, DT2216. Only the constructs with both modalities—*i.e.*, for
129 target and E3 ligase binding—function as BCL-x_L degraders in cells.
130

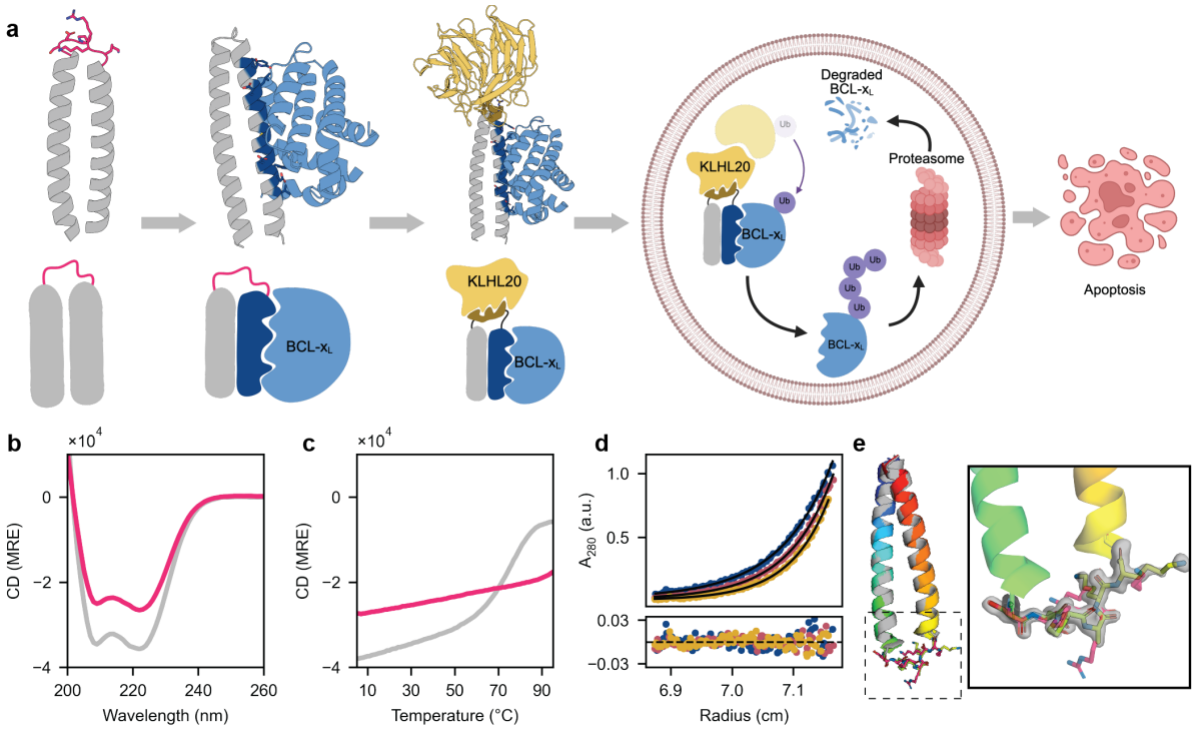

Figure 1: *De novo* design of a scaffold for display of multiple binding motifs. a, Schematic overview of this work. From left to right: helix-loop-helix scaffold (sc-apCC-2) designed based on the heterodimeric, antiparallel, coiled-coil peptides, apCC-Di-AB peptide[45]; grafting of the BCL-x_L binding site; addition of a second interaction site for the E3 ligase adapter, KLHL20, into the loop; and testing for BCL-x_L degradation and apoptosis in human cell lines. **b**, Circular dichroism (CD) spectra for apCC-Di-AB (grey) and sc-apCC-2 (magenta). CD spectra were recorded at 20 ºC and 50 µM total peptide/protein concentrations. **c,** Thermal response of CD signals at 222 nm for apCC-Di-AB (grey) and sc-apCC-2 (magenta), at 50 µM and 10 µM, respectively. **d,** Sedimentation-equilibrium analytical ultracentrifugation measurements at 52,000 RPM (blue), 56,000 RPM (red) and 60,000 RPM (yellow). The ratio between experimentally fitted and theoretical mass was 0.9 over the three speeds. **e,** X-ray crystal structure of the sc-apCC-2 scaffold, electron density around the loop shown at sigma level 1 (PDB id: 9TLL; 1.5 Å). Parts of this figure were made with BioRender.

RESULTS

Rational design yields a highly stable display scaffold

To create a small, highly thermostable and, highly designable scaffold for displaying helical target-binding sites and additional sites for E3 recruitment, we applied our rationally seeded peptide-to-protein approach[44]. Specifically, we generated a helix-loop-helix scaffold from a previously characterised antiparallel, heterodimeric *de novo* coiled coil, apCC-Di-AB[45]. Starting with the X-ray crystal structure of apCC-Di-AB, motif searching with MASTER[46] was used to find loops from the PDB to connect the two helices. Next, the sequence of one loop and flanking residues was optimized for the scaffold using Rosetta remodel[47] (Supplementary Fig. 1). Initially, this designed hairpin was made by Fmoc-based solid-phase peptide synthesis. Unlike the dimeric parent peptide, this was highly thermostable by CD spectroscopy. An X-ray crystal structure at 1.5 Å resolution (PDB id: 9TLL) had an overall backbone RMSD of 0.36 Å

158 between the design model and experimental structure, and it confirmed to the loop design. We
159 called this new 67-residue miniprotein scaffold, sc-apCC-2, using our systematic naming
160 system[44].
161

162 **ProteinMPNN-embellished motif grafting gives robust binders to the POI**

163 Previously, we have shown that dimeric coiled-coil peptides can bind to BCL-2 family proteins
164 by grafting hot-spot residues onto the outer helical surfaces[48,49]. To improve on this, we added
165 modern AI tools such as ProteinMPNN[26] and AlphaFold2[23] to the following computational
166 design pipeline, which is depicted in Fig. 2a. To seed binder designs, first, we examined
167 experimental structures of natural binders and targets in the BH3-only BCL-2 family and
168 identified six hot-spot positions. To generate starting sequences for these sites, we used a
169 small amino-acid pallet reflecting the sequences of BCL-2 effector proteins. For example, to
170 target BCL-X_L binding, we started with 18 different sequence motifs (Supplementary Table 10)
171 and grafted these onto 3 plausible locations on the solvent-exposed surface of the *de novo*
172 scaffold. Models for each of the resulting 54 seed sequences were aligned onto 5 models for
173 BCL-x_L:effector complexes where the pose of effector peptide was rotated incrementally by
174 10º (Supplementary Fig. 2), leading to 270 models. Next, to explore the potential to extend
175 the complementary binding surfaces, we applied ProteinMPNN-RosettaRelax protocols[26] and
176 varied the number of residues in the scaffold to be mutated. This yielded 609 different
177 sequences. For each of these, AlphaFold2 was used to predict complexes with BCL-x_L. These
178 models were filtered and assessed based on pLDDT, different AlphaFold2 metrics, shape
179 complementarity (Sc),[50] and Rosetta energy (ΔG)[51] to select candidates for experimental
180 testing. We repeated this protocol for MCL-1 as a secondary target. While also a member of
181 the BCL-2 family, it has a distinct selectivity profile and frequently shows increased levels as
182 a response to BCL-x_L inhibition[52].

183 We chose 14 designs against the primary target BCL-x_L and 4 against MCL-1 for
184 expression from synthetic genes in *E. coli*. All but one of these could be purified as soluble
185 protein, and the remaining 13 were highly thermostable helical proteins (Supplementary Fig.
186 3). X-ray crystal structures revealed that the surface mutations were accommodated by the
187 scaffold (PDB ids: 9TLM, 9TLN, 9TLO, 9TLP, 9TLQ, 9TLR, Supplementary Fig. 4-5). Initial
188 binding to both targets was probed using a competitive fluorescent anisotropy (FA) assay with
189 the natural effector peptide, BID, as the labelled competitor peptide that was displaced (K_D =
190 71 nM against BCL-x_L and K_D = 21.5 nM against MCL-1, Supplementary Fig. 6 and
191 Supplementary Table 11)[48,49]. 12 of the expressed designs had sub-μM IC_{50} values against
192 their intended targets, near the edge of the dynamic range for this assay (Supplementary Table
193 12). The MCL-1-targeting sequences were highly selective, while nearly all BCL-x_L targeting
194 designs bound both targets equally.

195 Isothermal titration calorimetry (ITC) was used to validate BCL-x_L binding for a selected
196 binder, Sc-apCC-2-BCL-x_L-3. This binder had an IC_{50} of 196 ± 14 nM by FA, and a K_D of 3 nM
197 at 37 °C by ITC (Fig. 2d and Supplementary Table 14). A 3 Å resolution X-ray crystal structure
198 for this complex revealed that side chains in the binding interface matched the predicted
199 conformation (Fig. 2e; PDB id 9TLU, 3.0 Å). Crystal structures of two MCL-1 binders in complex
200 with the target were also obtained (Fig. 2f and Supplementary Fig. 7; PDB ids 9TLV, 9TLW),
201 likewise confirming the accuracy of the designs and AlphaFold2 predictions.

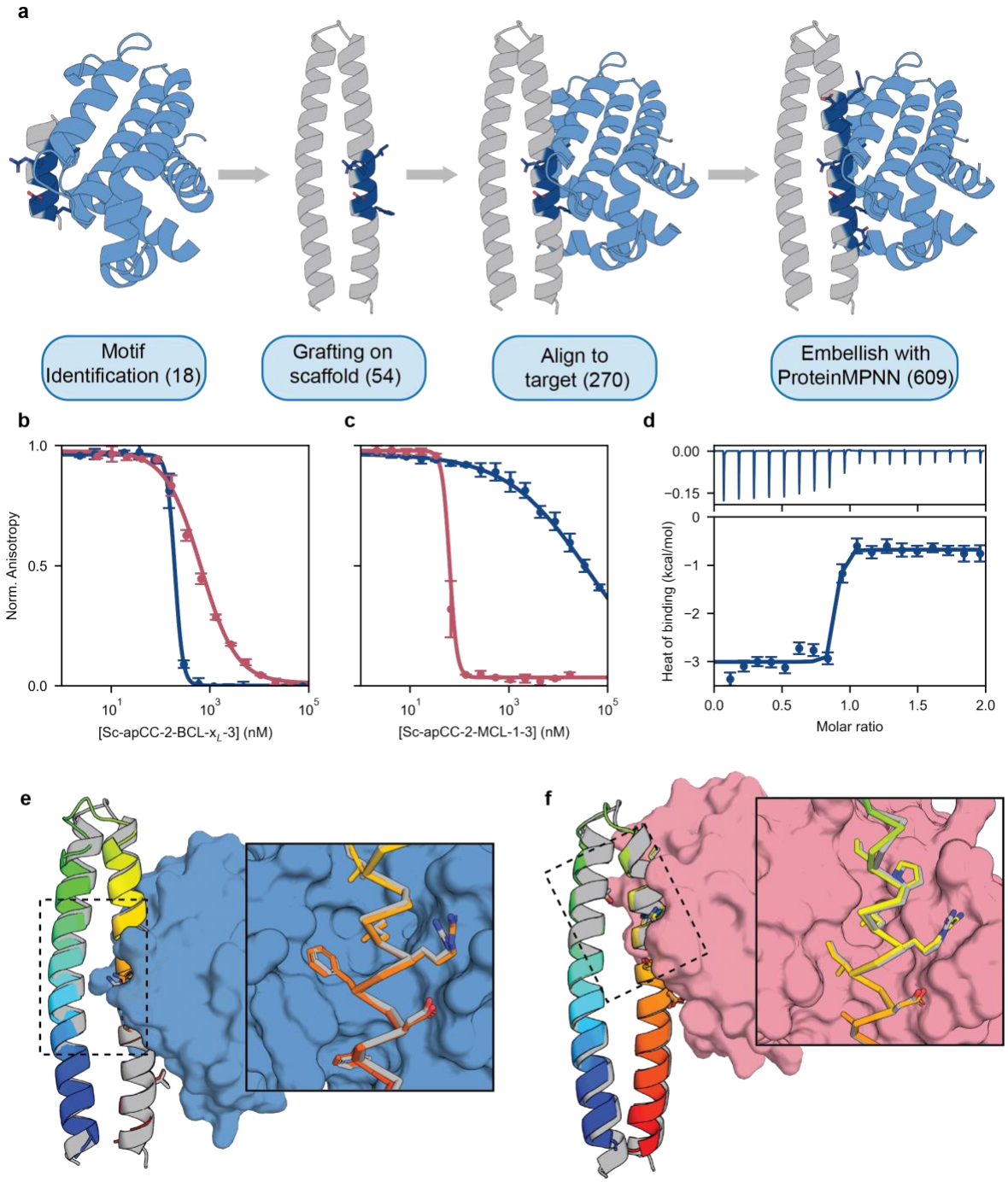

202

203 **Figure 2: *De novo* designed binders for BCL-2-family proteins. a**, Design schematic. From
204 left to right: hot-spot residues selected from natural BCL-x_L and MCL-1 effectors were grafted

onto the scaffold at all feasible surface-exposed locations of the scaffold and then aligned to the binding cleft; ProteinMPNN was used to add residues at the interface to improve binding. All final designed sequences were predicted as complexes with the target using AlphaFold2. Numbers in brackets refer to the motifs/designs at each step in the pipeline. **b**, Fluorescence anisotropy (FA) data for a BCL-x_L binder against BCL-x_L (dark blue, IC_{50}: 196 ± 14 nM) and MCL-1 (red, IC_{50}: 660 ± 50 nM). **c**, Similar FA data for a MCL-1 binder against MCL-1 (red, IC_{50}: 64 ± 2 nM) and BCL-x_L (dark blue IC_{50}: 40 ± 20 μM). **d,** ITC data and analysis for the BCL-x_L binder against BCL-x_L (K_D: 3 nM. **e,** Co-crystal X-ray structure of the BCL-x_L binder with BCL-x_L (PDB id 9TLU). The experimental structure of the sc-apCC-2 component (shown in rainbow colours) is aligned with its predicted model (grey), and the experimental structure of BCL-x_L is rendered as a surface (blue). The zoom shows details of the interacting side chains, the non-interacting helix and side chains are not shown for clarity. **f,** Similar images to **e**, but for the co-crystal X-ray structure of the MCL-1 binder and MCL-1 (PDB id 9TLV). The scaffold components in **e** and **f** are aligned vertically to highlight the shift in the designed binding sites.

Computational negative selection improves selectivity for the POI

Presumably due to the similarity between the peptide-binding interfaces on MCL-1 and BCL-x_L, the designed BCL-x_L binders showed little specificity. To improve this, we added the following computational negative-selection step as follows to identify selective designs for BCL-x_L. AlphaFold2 was used to model the complexes of all previously designs with both target proteins (Fig. 3a). These models were then scored and ranked based on the pLDDT of the motif residues, overall pAE score, and Sc. Sequences with large differences in rank for each metric and a combined metric were selected (Fig. 3b, and Supplementary Fig. 8). In total four further designs targeting BCL-x_L and two for MCL-1 were expressed in *E. coli*. Five of these could be purified as soluble proteins. Their biophysical characteristics were similar to the foregoing designs (Supplementary Fig. 9). From the FA assay showed that, the BCL-x_L binder selected by Sc, Sc-apCC-2-BCL-x_L-17, retained a high affinity for BCL-x_L and, moreover, it bound MCL-1 >1000-fold more weakly (Fig. 3c). The other designs selected using the other metrics—pLDDT and pAE, and a combination of these plus Sc—either showed little specificity or had decreased affinity for both targets (Supplementary Fig. 7 and 8). Thus, ProteinMPNN-enhanced motif grafting with some filtering—in this case based on shape complementarity scores—can generate tight and selective binders. That said, while the number of designs tested here is limited, these data suggest that current confidence-based metrics do not reliably distinguish between candidates for experimental testing. Further work is needed to assess computational designs more effectively, and to make pipelines like those outlined here more predictive.

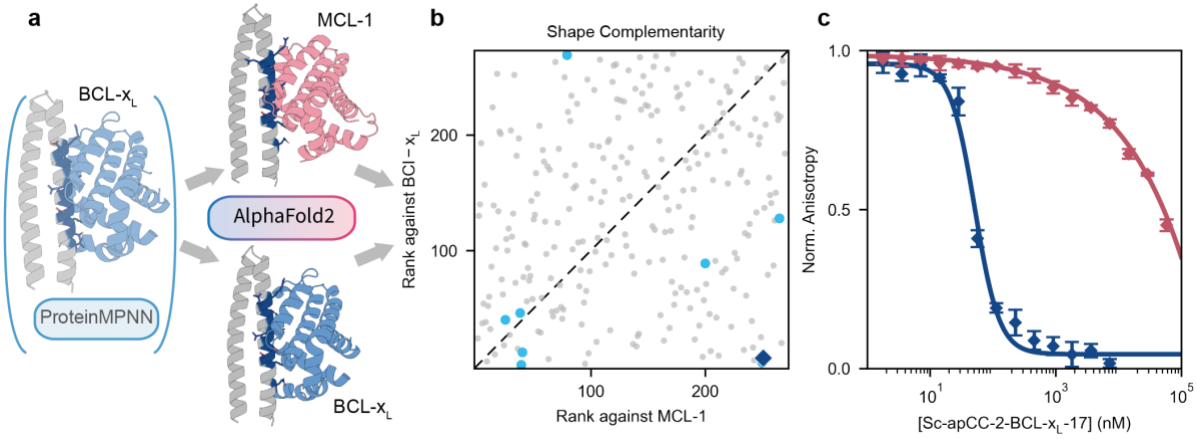

Figure 3: Designing selective binders for BCL-x_L through computational negative selection. a, Schematic of the selectivity procedure. After the ProteinMPNN design step against the desired target, AlphaFold2 was used to predict the complex with both targets, MCL-1 (red) and BCL-xL (blue). **b,** Designs were ranked for binding to both targets based on metrics such as shape complementarity (Sc, shown in this scatterplot; for others supplementary Fig. 6). Designs predicted to be selective for BCL-x_L are located in the bottom right corner. The designs selected based on Sc is shown as a dark blue diamond, and all previously tested anti-BCL-x_L designs as cyan circles. **c,** FA data for the BCL-x_L selective sequence based on Sc, binding data against BCL-x_L (dark blue, IC_{50}: 52 ± 3 nM) and MCL-1 (red, IC_{50}: 68 ± 80 µM).

E3 targeting by grafting a SLiM for KLHL20 into the designed loop

With potent BCL-x_L binders in hand, we turned to E3 targeting. The SLiM for KLHL20 adopts a turn-like conformation upon binding[43]. Therefore, we hypothesised that grafting the SLiM into the loop between the two helices of sc-apCC-2 might promote an active conformation and improve binding affinity. We replaced the loop with either the natural SLiM in two different lengths (short, 5 residues; or long, 11 residues) based on previous studies of KLHL20 binding[43], and we predicted models for the complexes with KLHL20 using AlphaFold2. Encouragingly, the positions of the SLiM hot-spot residues matched those in a known KLHL20/DAPK1 peptide complex[43]. However, the confidence of these initial predictions was low with pLDDT of the grafted motif <60. Therefore, we applied the ProteinMPNN-RosettaRelax protocol keeping the four central hot-spot residues of the SLiM fixed. This increased the pLDDT to >90 (Fig. 4a). Both the natural and optimised sequences were tested experimentally with two designs for each length. Biophysical characterisation and crystal X-ray structures confirmed that the SLiM-based loops were tolerated (PDBs id 9TLS, 9TLT, Fig. 4b and Supplementary Fig. 10 and 11). In a competitive FA-binding assay for KLHL20 binding, all designs had low micromolar IC_{50} values, (direct titration of the tracer indicated a K_D of 12 µM, see Supplementary Fig. 5, similar to previous reports[43]). Thus, the SLiM binding sequence can be grafted into the loop of sc-apCC-2 to yield KLHL20 binders without compromising other scaffold properties. Although the designs with the longer, 11-residue loops had higher affinities as did the ProteinMPNN-optimised designs relative to the natural sequences, the differences

277 were small with all IC_{50} values in the low µM range (Supplementary Fig.10; Supplementary
278 Table 13).
279

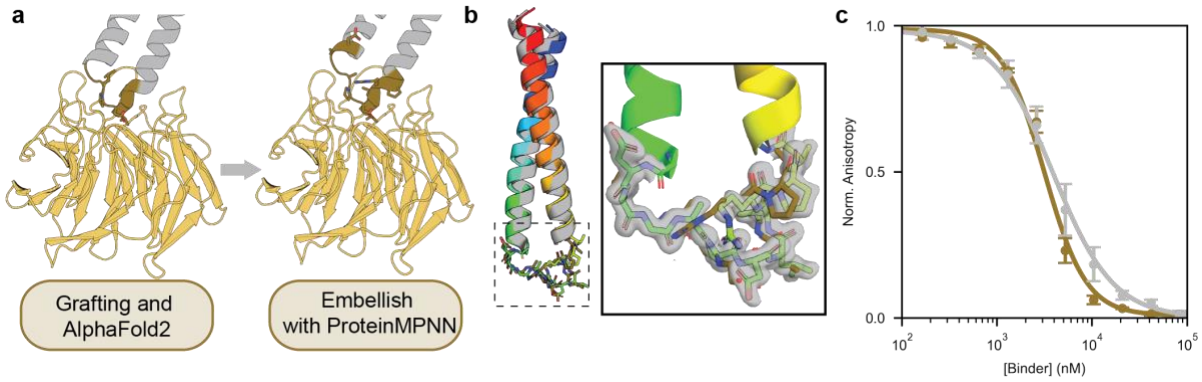

280
281 **Figure 4: Incorporation of a SLiM for E3 ligase recruitment into the *de novo* scaffold.**
282 **a**, A natural SLiM sequence (brown) was grafted into the loop of the scaffold, and AlphaFold2
283 used to predict the complex with the recognition domain of KLHL20. ProteinMPNN was used
284 to alter residues close the target. **b,** X-ray crystal structure of the sc-apCC2-KLHL20-3
285 (ProteinMPNN short-loop design; PDB id 9TLS), electron density shown around the loop at
286 sigma level 1. **c,** FA data for KLHL20 binding with the natural short-loop design (grey) (IC_{50}:
287 3.9 ± 0.2 µM) and the ProteinMPNN short-loop design (brown) (IC_{50}: 3.16 ± 0.18 µM).
288

289 **BCL-x_L and KLHL20 binders recruit their targets in a GFP-based degradation assay**

290 To test the capacity of the monofunctional BCL-xL and KLHL20 binders to recruit their targets,
291 we used a previously established GFP-based degradation assay HEK293 cells (accompanying
292 paper). The assay follows degradation of transiently expressed protein and allows a medium-
293 throughput assessment of individual binders to inform those that could be combined in single
294 construct. In brief, to test the BCL-x_L binders, HEK293 cells engineered to express a BCL-
295 x_L:GFP fusion protein stably were transfected with BCL-x_L binders fused to the full-length
296 SPOP E3 ligase. 4 out of 8 binders showed significantly decreased GFP fluorescence
297 compared to the negative control. To test the KLHL20 binders, the same HEK293 cells were
298 transfected with the KLHL20 binders fused to an anti-GFP nanobody. All 4 binders lowered
299 GFP fluorescence (see Supplementary. Fig. 12).
300

301 **Bifunctional designs are potent degraders of BCL-x_L and induce apoptosis**

302 After validating their degradation capacity individually, we combined the BCL-xL and KLHL20
303 binding sites into a single scaffold, and we tested for endogenous BCL-x_L degradation in a
304 lung-cancer cell line (A549). For this, we chose the most potent and best performing BCL-x_L
305 binder from the GFP-based degradation assay, sc-apCC2-BCL-x_L-5, and combined it with the
306 KLHL20-binding module, sc-apCC2-KLHL20-3. These were configured in two ways (Fig. 5a):
307 one with two binding motifs combined within a single coiled-coil module; and a second with the
308 two monofunctional modules linked in tandem (Supplementary Fig. 13). For negative controls

309 we used both *de novo* binding proteins individually. As a positive control we used PROTAC
310 DT2216, which comprises small-molecule ligands for BCL-x_L and VHL (Supplementary
311 Fig.14). A fluorescently labelled anti-BCL-x_L antibody was used to measure endogenous BCL-
312 x_L levels. Neither of the separate monofunctional controls significantly decreased BCL-x_L levels
313 (Fig. 5b&d. However, both bifunctional designs showed significant decreases in BCL-x_L, just
314 as DT2216 (Fig. 5b&d). Addition of the proteasome inhibitor carfilzomib decreased the level of
315 degradation significantly, indicating a proteasome-depended mechanism (see Supplementary
316 Fig. 15). Combinations of other BCL-x_L and KLHL20 binding sequences yield similar results,
317 highlighting the versatility of the scaffold and the binding site design (Fig. 5d and
318 Supplementary Fig. 16).
319

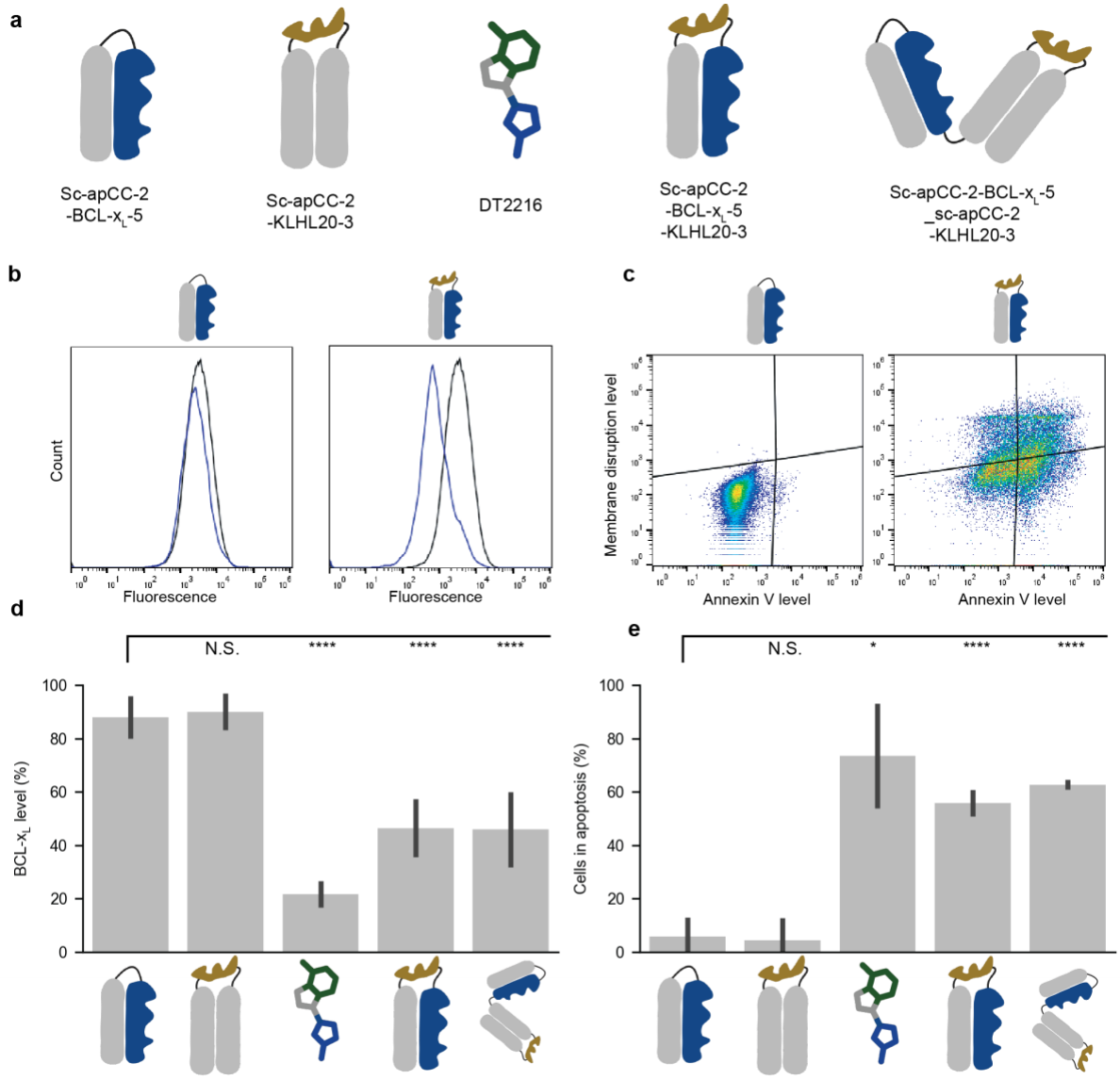

320

321 **Figure 5**: **Bifunctional binders cause endogenous BCL-x_L degradation and apoptosis. a,**
322 Schematic of the molecules tested. All the designs use the same BCL-x_L- and KLHL20-binding
323 motifs. Negative controls are monofunctional (*i.e.*, contain only the BCL-x_L-binding motif (blue)
324 or the KLHL20-binding motif (brown). Small-molecule PROTAC DT2216 was used as a

325 positive control (the chemical structure is only a cartoon representation). **b,** Flow cytometry
326 results for the endogenous degradation, representative results for the negative control and
327 combined binders are shown. Histograms for design (blue) and mCherry control (black). **c,**
328 Flow cytometry results for the apoptosis assay Annexin V level on the x-axis, and DAPI signal
329 indicating membrane disruption on the y-axis. Representative results are shown for negative
330 control and combined binder. **d,** Degradation assay for native BCL-x_L in the A549 cell line.
331 BCL-x_L levels were calculated by the Overton positive method, average of at least three
332 biological repeats. Significance levels calculated with Welch t-test against the BCL-x_L binder.
333 **e,** Apoptosis assay, bars show combined early and late apoptosis averaged over at least three
334 biological repeats. Significance levels calculated with a Welch t-test against the BCL-x_L binder.
335 Significance levels are represented as N.S.: $P > 0.05$, $*$: $P \leq 0.05$, $****$: $P \leq 0.0001$. Parts of
336 this figure were made with BioRender.
337

338 Depleting BCL-x_L should increase apoptosis. To test this, we used another 2D FACS
339 assay to measure (i) externalised phosphatidylserine indicative of early-stage apoptosis using
340 FITC-labelled Annexin V (x-axis), and (ii) cell viability using DAPI to monitor loss of membrane
341 integrity associated with late-stage apoptosis (y-axis)[53] (Fig. 5c). Overall apoptosis (combined
342 early and late) mirrored the protein-degradation assay (compare Fig. 5c&e): the individual
343 binders did not increase apoptosis above baseline, whilst the bifunctional helix-loop-helix
344 constructs showed significant increases, comparable to the addition of DT2216. These results
345 were mirrored in a ApoTox-Glo™ Triplex Assay, which assesses cell viability, cytotoxicity and
346 apoptosis events simultaneously (Supplementary Fig. 17). Combined, these experiments
347 show that transfection of bifunctionalised scaffolds into live cells causes robust degradation
348 and subsequent induction of apoptosis on a par with the small-molecule PROTAC.
349

350 **DISCUSSION**

351 In summary, to develop *de novo*-protein-based PROTACs, we report the computational design
352 of a small, highly stable protein scaffold to present multiple epitopes that engage different
353 subcellular proteins. Using this, we introduce a binding site for the anti-apoptotic, cancer target
354 BCL-x_L and another for an E3 ubiquitin ligase, KLHL20. Effectively, this produces a *de novo*
355 protein based PROTAC that brings these proteins together in cells. Indeed, the bifunctional
356 proteins do cause degradation of BCL-x_L and increase apoptosis in a cancer cell line. The
357 designed proteins are characterised fully *in vitro* allowing them and the design methods to be
358 evaluated.

359 Recently, the incorporation of multiple, independent binding sites into a single *de novo*
360 scaffold has been reported[31]. Moreover, others have combined engineered or designed
361 proteins to render the EndoTag and GPlad systems for clearing proteins by internalisation into
362 cells, or via modification followed by proteolysis within cells, respectively[32,33,54]. In The
363 PROTAC field polypeptides have long been used as modules[7]. Recently, protein design tools
364 such as RFDiffusion[25] and ProteinMPNN[26] have been used to generate bifunctional
365 unstructured peptides that bind the androgen receptor and the E3, VHL, leading to degradation

366 of the former[55]. The design of a structured helical dimer comprising a SOS mimetic and p53
367 mimetic within a crosslinked dimer has been shown to engage MDM2 E3 ligase, and reduce
368 levels of RAS[56]

369 Our designs are distinct from the peptide-based systems, as they are stable, folded
370 proteins that simultaneously bind a target and an E3 ligase. Nonetheless, they still allow the
371 flexible introduction of different binding sites by grafting onto structured helical surfaces or
372 within the constrained loop. This promises opportunities in future to screen target—E3 pairings,
373 and to direct the orientation of the bound proteins for tailored ubiquitination. This *de novo*
374 design approach also offers possibilities for generating proteins that intervene in and direct
375 other post-translational modifications such as phosphorylation[57].

376 Our approach also facilitates full biophysical and structural characterisation of the
377 designs, as demonstrated by several co-crystal structures that we report here. In turn, this
378 helps critically assess the designs and design methods. For instance, we use motif grafting
379 embellished with computational sequence design using ProteinMPNN followed by AlphaFold2
380 structure predictions. In almost all cases, the addition of residues in direct contact with the
381 targets improves the AlphaFold2 and physical-scoring metrics. Interestingly, and as reported
382 by others[26,27] extending ProteinMPNN to residues outside of the binding site improves the
383 AlphaFold2 confidence metrics but does not alter the physical scoring metrics untouched
384 (Supplementary Fig. 19). Moreover, improvements suggested by *in silico* modelling and
385 assessment are not necessarily reflected in experimental measurements of binding constants.
386 For instance, for the BCL-2-family binders, extending the binding site beyond the natural, hot-
387 spot motif proved essential to achieve better binding; however, when targeting the KLHL20-
388 binding site there was no improvement beyond using the natural (SLiM) sequence. This raises
389 the potential problem of false positives in design pipelines. Moreover, and aligned with recent
390 large-scale *de novo* binder studies[58] and other benchmarks[59], we find that none of the AI
391 confidence predictors or physical scoring metrics correlate well with the measured
392 experimental binding affinities (Supplementary Fig. 20-24). Thus, in our view and corroborated
393 by others[58-60], the development of better *in silico* predictors of binding affinity, or simply better
394 ranking schemes for the best binders to test experimentally are key and important challenges
395 for the *de novo* design field.
396
397 **MATERIALS AND METHODS**
398
399 **Computational loop design**
400 The last and first six residues from the A and B chain of the previously published crystal
401 structure of apCC-Di-AB (PDB:7Q1T) respectively were used as a search query for
402 MASTER[46]. The original database made available with the publication was used. Results up

403 to 0.6 Å RMSD were separated by the number of residues in between the helices. Loops of 4
404 residues were the most common and the lowest RMSD hit (PDB id 2XPI residues 470-473)
405 was chosen as the starting structure for remodelling. Starting from the aligned and inserted
406 loop, 100 Rosetta remodel[47] trajectories were run, a total of 6 residues (the 4 loop residues
407 and 2 flanking residues) were mutated to any amino acid but cysteine. The remaining
408 sequence was fixed. The lowest energy model was selected for experimental testing.

409 **Computational binding site design**

410 For the BCL-x_L binder design, a selection of 6 residue motifs based on the natural binders
411 (BAD and BIM) were created. All motifs have the following structure Φ_1...L..Φ_2XD.F with
412 Φ_1 either Y,F or I, Φ_2 either F,I,M and X either G,S. The full list of motifs is shown in
413 supplementary table 10. These motifs were grafted onto a modified model of sc-apCC-2, so
414 that none of the core coiled-coil heptad positions (**a** and **d**) were altered. To accommodate the
415 binding sites better, 4 residues were added to each helical termini, the R@**a**, D@**e** pairs were
416 split and charges were more evenly distributed at **e** and **g** heptad positions as is the case in
417 apCC-Di[45]. This scaffold could accommodate the motifs at 3 locations resulting in a total of 54.

418 These models were aligned on 5 slightly modified AlphaFold2 predictions of natural
419 effector:protein complexes. A Rosetta script introduced a small angular shift in the effector
420 binding angle, the resulting 5 models are shown in supplementary figure 2. Subsequently, 4
421 different strategies were used to modify the sequence with a ProteinMPNN-RosettaRelax
422 pipeline: Strategy 1, no additional mutations were made; Strategy 2 non-motif, non-core and
423 non-loop residues within 6 Å from BCL-x_L are allowed to mutate; Strategy 3 all non-motif, non-
424 core and non-loop residues are allowed to mutate; Strategy 4 all non-core residues are allowed
425 to mutate (thus including the natural motifs and designed loop). The ProteinMPNN-
426 RosettaRelax pipeline consisted of 3 cycles of ProteinMPNN at a temperature of 0.2, grafting
427 of the top sequence onto the helix-loop-helix and a short relax following the
428 InterfaceRelax2019 script. After the final relax run, Rosetta scores including shape
429 complementarity and interface ΔG were calculated. In addition, an AlphaFold2 prediction was
430 made of each final sequence with and without a pre-generated MSA of BCL-x_L. Designs were
431 filtered based on pLDDT (>85 as a monomer and >90 as a complex) and a final selection was
432 made based pLDDT, pAE, ΔG or shape complementarity. All selected sequences with their
433 respective strategy and selection method are shown in supplementary table 4.

434 For MCL-1, the same method was employed but only the MPNN implementation in strategy 2
435 was used. Instead of strategy 1, the entire previously described binding site[48] was grafted onto
436 the modified sc-apCC-2 model. Selected sequences are shown in supplementary table 3.

437 For KLHL20, the previously designed loop was replaced with the natural SLiM sequences -
438 AGLPDLVGA- (short) or -AGLGLPDLVAKYNGA- (long). AlphaFold2 models were predicted
439 with a pre-genrated MSA for KLHL20. Subsequently the same three cycle ProteinMPNN-
440 RosettaRelax pipeline was used keeping the middle -PDLV- of the SLiM fixed.

441 All code and inputs are available from the labs Github page.

442 **Computational selectivity screening**

443 For the BCL-x_L and MCL-1 selectivity screening, AlphaFold2 predictions were made of the final
444 sequences of strategy 2 with the opposite target's MSA. In addition, the final sequences were
445 grafted on sc-apCC-2 and target complexes and subsequently relaxed and scored by Rosetta.
446 For pLDDT, pAE and Shape Complementarity the rank of each sequence against each target
447 was determined, sequences with the largest difference in rank favouring the desired target
448 were selected. All code and input are available from the labs Github page.

449 **Solid-phase peptide synthesis and purification**

450 All peptides used in this study (see Supplementary Table 1) were synthesised following
451 standard Fmoc automated microwave solid-phase peptide synthesis procedures with a Liberty
452 Blue (CEM) as descripted before[44,49]. N,N'-diisopropylcarbodiimide (DIC) and Oxyma Pure in
453 N,N-dimethylformamide (DMF) were used as activators and a 20% (v/v) solution of morpholine
454 or piperidine in DMF was used in the deprotection step. Peptides with acetyl (Ac) caps were
455 treated with pyridine or diisopropylethylamine and acetic anhydride. 5-carboxyfluorescein
456 (FAM) coupled peptides were prepared by coupling of 6-(amino)-hexanoic acid and FAM with
457 the standard DIC and Oxyma Pure in DMF mixture. Peptides were cleaved from the resin with
458 a trifluoracetic acid (TFA):water:triisopropysilane mixture in 95:2.5:2.5 (v/v) ratio at room
459 temperature. Subsequently, cleaved peptides were precipitated with ice-cold diethyl ether.

460 The freeze-dried peptides were dissolved in a water/acetonitrile mixture and purified with
461 reverse-phase HPLC using Water and acetonitrile with 0.1% (v/v) TFA as solvents. Peptide
462 purity was assessed by analytical HPLC (see Supplementary Fig. 25, 31, 33, 35, 37), and
463 matrix-assisted laser desorption/ionization-time of flight (MALDI-TOF) mass spectrometry (see
464 Supplementary Fig. 25, 30, 32, 34, 36).

465 **Protein expression and purification**

466 The genes encoding the designed binders and target proteins (BCL-xL, MCL-1) were cloned
467 into a pet28a vector with Kanamycin resistance. E. coli BL21 DE3 cells were transformed with
468 the plasmids (see Supplementary Tables 2-7 for protein sequences). Cells were grown in Luria
469 Broth at 37º C until an optical cell density of 0.6 was reached. Protein production was induced

470 by addition of isopropyl-β-D-thiogalactoside and cultures were kept at 20 ºC overnight.
471 Afterwards, the cells were harvested by centrifugation and frozen until further use.
472
473 For purification of the binders, the cells were resuspended in binding buffer (25 mM Tris, 300
474 mM NaCl, 10 mM imidazole pH 8.0) and lysed by sonication. The lysate was clarified by
475 centrifugation. The supernatant was applied on a His-trap column equilibrated with binding
476 buffer and washed with (30 mM imidazole. The protein was eluted with 300 mM imidazole.
477 Subsequently, the imidazole was removed by a PD-10 desalting column and incubated
478 overnight with TEV protease at room temperature. After His-tag cleavage, the protein solution
479 was reapplied on the His-trap column and flow-through was collected. This flow-through was
480 applied on a HiLoad 16/600 superdex75 column equilibrated in biophysics buffer (25 mM Tris,
481 150 mM NaCl, pH 7.4). The peak containing the monomeric proteins was collected and
482 concentrated for later use.
483
484 For BCL-xL and MCL-1 protocols were followed as previously described[49]. The cells were
485 resuspended in lysis buffer (25 mM Tris, 500 mM NaCl, pH 8.0 cOmplete, Mini, EDTA free
486 protease inhibitor cocktail, Roche and 5 mg lysozyme and 3 mg DNAse, Roche). Afterwards,
487 they were sonicated and clarified via centrifugation. The soluble fraction was applied on a His-
488 trap HP column (Merck) pre-equilibrated with wash buffer (10 mM imidazole, 25 mM Tris, 500
489 mM NaCl, pH 8.0). The column was then washed four times with increasing concentration of
490 imidazole up to 100 mM, before a final elution with 400 mM imidazole. The protein solution
491 was dialyzed overnight together with His-Ulp1 to remove the SUMO-tag. The next day the
492 solution was applied on the His-trap HP column and the flow-through was collected. This flow
493 through was collected and passed-through size exclusion chromatography with a HiLoad
494 26/60 Superdex 75 column. This column was previously equilibrated with 20 mM Tris 250 mM
495 NaCl, 0.5 mM DTT, 2.5% glycerol, pH 8.0. The fractions containing the monomeric protein
496 were pooled and concentrated before storage for later use. Protein purity and quality was
497 assessed by mass spectrometry (see Supplementary Fig. 26-27) and CD (see Supplementary
498 Fig. 29).
499
500 For KLHL20 expression and purification, Rosetta™ (DE3) Competent Cells (Novagen) were
501 transformed with a KLH20 DNA construct (pNIC28-Bsa4-6his-KLHL20(303-605). Cells were
502 grown to OD600 of 0.6 at 37 ºC, before the temperature was lowered to 18 ºC and protein
503 expression was induced with 0.4 mM IPTG overnight. The cells were pelleted by centrifugation
504 and resuspended in lysis buffer (50 mM HEPES pH 7.5, 500 mM NaCl 5% glycerol, 0.5 mM
505 TCEP, 5 mg lysozyme, 3 mg DNAse and 1 cOmplete, Mini, EDTA free protease inhibitor
506 cocktail tablet). Afterwards, the cells were sonicated and clarified by centrifugation. The

507 supernatant was applied to 5 mL HisPur Ni-NTA resin (Thermo Fisher), preequilibrated with
508 binding buffer (50 mM HEPES pH 7.5, 500 mM NaCl, 5% glycerol, 0.5 mM TCEP) and left
509 rotating at 4 ºC overnight. The flow through was collected using a peristaltic pump and the
510 beads were washed four times with increasing imidazole concentration (10 mM -100 mM).
511 Subsequently, the protein was eluted with 300 mM imidazole in the same buffer. The eluted
512 protein was dialyzed overnight with TEV protease, before being applied again on the Ni-NTA
513 beads. The cleaved KLHL20(303-605) was eluted with the same elution buffer. The protein
514 was dialyzed into 50 mM HEPES pH 7.5, 300 mM NaCl, 0.5 mM TCEP, 2.5% (v/v) glycerol
515 and concentrated before storage for later use. Protein purity and quality was assessed by
516 mass spectrometry (see Supplementary Fig. 28) and CD (see Supplementary Fig. 29).

517 **Circular dichroism spectroscopy**

518 Circular dichroism (CD) spectroscopy data were collected on a JASCO spectropolarimeter
519 instrument fitted with a Peltier temperature controller. The binders were prepared to 20 µM
520 concentration in 20 mM Tris 150 mM NaCl, pH 7.4 buffer unless otherwise stated in figure
521 legends. Data were collected in a 1-mm quartz cuvette with a 200 nm to 260 nm wavelength.
522 The following instrument settings were used: band width, 1 nm; data pitch, 1 nm; scanning
523 speed, 100 nm/min; response time 1 s. Each spectrum is the background subtracted average
524 of 8 scans. For the thermal denaturation scans, the circular dichroism signal was followed at
525 222 nm wavelength while increasing the temperature from 5 ºC to 95 ºC at a ramp rate of 1
526 ºC/min. BCL-x_L, MCL-1 and KLHL20 were measured in 10 mM K_2HPO_4 adjusted with NaOH
527 to pH 7.4 at 50 µM protein concentration. The spectra were normalized to mean residue
528 ellipticities (deg cm^2 $dmol^{-1}res^{-1}$) by normalizing for concentration of peptide bonds and the cell
529 path length using equation MRE = $\frac{\theta \times 10^6}{c \times l \times n}$ with θ the measured difference in absorbed circularly
530 polarized light in mdeg, *c* the concentration in µM, *l* the path length in mm and *n* the number
531 of amide bonds in the proteins.

532 **Analytical size exclusion chromatography**

533 Analytical size exclusion chromatography was performed on a JASCO HPLC system with a
534 superdex 75 increase 10/300 column. 20 µL of protein solution at a concentration of 100 µM
535 in 20 mM Tris, 150 mM NaCl, pH 7.4 was injected at 0.5 mL/min. The UV absorbance at 230
536 nm was recorded, the background was subtracted and the normalized signal was plotted in
537 function of elution volume.

538 **Analytical ultracentrifugation**

539 Sedimentation equilibrium experiments were performed on a Beckman Optima X-LI analytical
540 ultracentrifuge with an An-60-Ti rotor (Beckman-Coulter) and data was fitted using SEDPHAT
541 software[61] to single-species model. Monte Carlo analysis was performed to yield 95%

542 confidence limits. A peptide concentration of 100 μM in PBS (8.2 mM sodium phosphate
543 dibasic, 1.8 mM potassium phosphate monobasic, 137 mM NaCl, 2.4 mM KCl, pH 7.4) was
544 used. The sample was spun at 52000, 56000 and 60000 RPM after 8-hour equilibration at
545 each speed, the measurement at each speed was duplicated.

546

547 **Competitive fluorescence anisotropy assay**

548 The competitive fluorescence anisotropy experiment were performed following previously
549 described procedures[49]. Each experiment was run in triplicate and the fluorescence anisotropy
550 measured using a CLARIOstar plus plate reader (BMG Labtech), with excitation at 482nm
551 (bandwidth = 16nM), emission at 530nm (bandwidth = 40nm) and polarised dichroic mirror at
552 504nm. For the direct titration assay, stock concentrations of 1mg/ml peptide were made in
553 DMSO and then further diluted to a working stock of 100nM in FA buffer (20mM tris, 150mM
554 NaCl pH7.4 1mM DTT 0.01% triton x100) for use in the assay. For MCL-1 and BCL-x_L
555 experiments, the target protein concentration was fixed at 150 nM and tracer concentration
556 fixed at 25 nM. For KLHL20 experiments, KLHL20 concentration was fixed at 8 μM and 83.3
557 nM tracer concentration. The competitor protein was titrated in.

558 Perpendicular (P) and parallel (S) intensities of the control wells were averaged and deducted
559 from each corresponding samples to give the corrected values, P_{corr} ($P_{corr} = P_{sample} – P_{av.\ control}$)
560 and S_{corr} ($S_{corr} = S_{sample} – S_{av.\ control}$). The total sample intensities (I) and anisotropies (r) were
561 calculated with the follow equations: $I = (2 \times P_{corr}) + S_{corr}$, $r = (S_{corr} – P_{corr}) / I$

562 The points for each competition curve were normalised between 0 and 1. The obtained values
563 were plotted against competitor concentrations and fit to a logistic function of the form $Y = A2
564 + (A1 – A2) / (1 + (x/IC_{50})^p)$ to determine the half-maximal inhibitory concentration (IC_{50}) of the
565 peptide competitor (where A2 is the upper asymptote and A1 the lower asymptote).

566 **Isothermal Titration Calorimetry**

567 Isothermal titration calorimetry (ITC) experiments were carried out using a MicroCal PEAQ-
568 ITC system (Malvern Panalytical) at 37 °C. A stock solution of BCL-xL was dialyzed into ITC
569 buffer overnight (20 mM Tris, 150 mM NaCl pH 7.4), and the same buffer was employed to
570 dissolve a solid portion of the tested binder. For each experiment, initially, the cell was filled
571 with 275 μl of binder (20 μM) and the syringe was loaded with the BCL-xL at 200 μM
572 concentration. An initial injection of 0.4 μL was then followed by 18 injections of 2 μL, every
573 150s, with a constant syringe rotation speed of 750 rpm throughout. The signal for the enthalpy
574 of dilution of the protein into buffer was independently measured in a control titration
575 experiment and then subtracted from the experimental binding traces. NITPIC[62] was used to

576 integrate the injections. The data was then fitted with SEDPHAT software[61] to extract K_D, ΔG°,
577 ΔH° and -TΔS° using an adjusted single-site binding model.

578 **Crystallisation trials**

579 Protein crystals were grown using a sitting-drop, vapor diffusion method with commercial
580 sparse matrix screens. 0.3 µL of a concentrated protein solution or 1:1 mixture of proteins in
581 case of the binders was mixed with 0.3 µL of the screening solution in MRC 96 well plates.
582 The plates were incubated at 20 ºC until protein crystals were observed. The crystallisation
583 condition for each structure can be found in Supplementary table 15. The crystals were
584 mounted and transferred to a cryoprotecting solution made of the screen supplemented to 25%
585 glycerol before flash freezing in liquid nitrogen.

586 The proteins were diffracted at Diamond light source or the European Synchrotron Radiation
587 Facility. Data processing was done on the beamline with either XDS[63] or Dials[64]. Aimless[65] was
588 used for scaling. Molecular replacement was done with PHASER[66] using AlphaFold2 models.
589 Phenix Refine[67] was used for refinement of the structures using translation/liberation/screw
590 (TLS) parameters for each chain. Data and refinement quality statistics can be found in
591 supplementary table 16.

592 **Cell culture**

593 All cell culture procedures were carried out according to standard procedures. In brief, all cell
594 lines were maintained at 37 °C in an atmosphere of 5% CO_2 and ≥95% humidity. HEK293T
595 cells were cultured in Dulbecco's Modified Eagle Medium (DMEM; Gibco™) supplemented
596 with 10% foetal bovine serum (FBS), while A549 cells were grown in Nutrient Mixture F-12
597 Ham medium (Merck) supplemented with 10% FBS. DNA transfections were performed using
598 the cationic lipid reagent TransIT-2020 (Mirus Bio).

599 Stable GFP–Bcl-x_L cell lines (see Supplementary Table 8) were generated in a previous study
600 (accompanying paper) through antibiotic selection followed by sorting of live GFP-positive cells
601 for subsequent propagation.

602 **Flow cytometry assay of degradation of GFP-BCL-x_L**

603 BCL-x_L binders were synthetized in pcDNA3.1Hygro(+) plasmid (GenScript) in such a way that
604 they are preceded by a single FLAG tag and followed by the SPOP E3 ligase and mCherry
605 with a T2A self-cleaving peptide sequence. The KLHL20 binder constructs were in the same
606 plasmid preceded by a FLAG tag and anti-GFP nanobody and followed by the same mCherry
607 T2A combination. Full protein sequences are found in Supporting Table 8.

608 The flow cytometry assay was performed as previously descripted (accompanying paper).
609 Briefly, on day 1, cells were seeded at a density of 300,000 per well supplemented DMEM

610 without antibiotics. On day 2, cells were transfected following the manufacturer's instructions,
611 with a ratio of 0.5 µg DNA to 1.5 µL transfection TransIT-2020. On day 4 (48 hours after
612 transfection), cells were washed with PBS, trypsinized, resuspended in FACS buffer and
613 stained with DAPI (1 µg/mL) prior to flow cytometry on a Attune NxT instrument (ThermoFisher
614 Scientific). The data was analysed with FlowJo v10. Events were gated based on fluorescence
615 of cells stably expressing GFP-BCL-x_L and transfected with an mCherry-only control (quadrant
616 Q2). Degradation of BCL-x_L was indicated by reduced GFP fluorescence intensity and a shift
617 to Q1. Results represent at least three independent experiments and are expressed as the
618 percentage of remaining GFP-BCL-x_L (100 x Q2/(Q1 + Q2) ± standard deviation). Statistics
619 were calculated using a two-sided Welsch's T-test. Significance levels are represented as
620 N.S.: $P > 0.05$, ∗: $P \leq 0.05$, ∗∗: $P \leq 0.01$, ∗∗∗: $P \leq 0.001$, ∗∗∗∗: $P \leq 0.0001$.

621 **Flow cytometry assay of endogenous BCL-x_L degradation**

622 The protein constructs for the endogenous degradation assays were in the same
623 pcDNA3.1Hygro(+) plasmid (GenScript). Constructs had N-terminal FLAG tag and were
624 followed by mCherry preceded by a T2A self-cleaving peptide.

625 The flow cytometry assay was performed as previously descripted (accompanying paper).
626 A549 cells were cultured as above and fixed in 4% formaldehyde 48 hours after transfection
627 or 48 hours after treatment with 1 µM concentration of DT2216 (#37311, Cayman Chemical).
628 Then, following a PBS wash the cells were permeabilized with cold methanol for 15 minutes
629 on ice and incubated overnight at 4 ºC with BCL-x_L (54H6) Rabbit mAb (Alexa Fluor 488
630 Conjugate) antibody and a Rabbit IgG Isotype control, Alexa Fluor 488 Conjugated (Cell
631 Signaling, BS-0295P-A488-BSS-100uL Startech Scientific Ltd, respectively). The cells were
632 washed and resuspended in PBS for flow cytometry measurements. For the proteasome
633 inhibitor experiments cells were treated with 20 µM carfilzomib for 24 hours prior to
634 measurements (Carfilzomib (PR-171), #A1933, APExBIO). The data was analysed with
635 FlowJo v10. Results were plotted as events of BCL-x_L Alexa 488 channel. The percentage of
636 cells that lost fluorescence was calculated by subtracting out the mCherry control using the
637 Overton positive method. Data are from at least 3 independent experiments Statistics were
638 calculated using a two-sided Welsch's T-test. Significance levels are represented as N.S.: $P >$
639 0.05, ∗: $P \leq 0.05$, ∗∗: $P \leq 0.01$, ∗∗∗: $P \leq 0.001$, ∗∗∗∗: $P \leq 0.0001$.

640 **Flow cytometry apoptosis assay**

641 The same DNA constructs as in the endogenous degradation assay were used. The flow
642 cytometry apoptosis assay was performed as descripted above (accompanying paper). Briefly,
643 48 hours before flow-cytometry measurements A549 cells were transfected with degraders or
644 treated with DT2216 at 1 µM (#37311, Cayman Chemical). Then, cells were detached, washed

645 with PBS and incubated for 30 minutes to allow recovery. Afterwards, the cells were stained
646 with FITC-conjugated Annexin V (BioLegend) in accordance with the manufacture's protocol
647 except for a longer 45-minute incubation time. Next, the cells were washed in 1x binding buffer
648 and resuspend in 300 µL of binding buffer containing DAPI (BD Pharmingen). Cells,
649 undergoing early apoptosis have externalized phosphatidylserine binding to Annexin in a
650 calcium-dependent manner. Cells in late-stage apoptosis lose membrane integrity and get
651 stained by DAPI. Apoptosis was calculated as the sum of cells in early and late stages and
652 expressed as percentage of total cell count.

653 **ApoTox-Glo™ Triplex Assay**

654 Viability, cytotoxicity and apoptosis assays were performed using the Promega kit according
655 to the provided protocols, with the exception of additional filters to eliminate the mCherry
656 fluorescence background; fluorescence filter wavelengths were 485 ± 10 nm for excitation and
657 520±20 nm for emission for the cytotoxicity measurements, and 400 ± 20 nm for excitation and
658 505±20 nm for emission for the viability measurements. Luminescence readings at 545±40 nm
659 were used for the apoptosis measurements.
660

661 **ACKNOWLEDGMENTS**

662 This work was primarily supported by grants from the BBSRC (BB/V006231/1, BB/V006703/1
663 BB/V008412/1, and BB/V008412/2), with additional support from BB/V003577/1,
664 BB/V003577/2 and BB/Y007816/1. X-ray diffraction experiments were supported by Diamond
665 beam time awarded under proposal number MX34438, MX31440 and MX37593 and ESRF
666 beamtime awarded under proposal number MX2373. DTH was supported by Cancer Research
667 UK core funding (A29252). We thank Alex Bullock for providing the plasmids enoding the
668 KLHL20 plasmid. We thank Simon Coulton and Andrew Lovering for assistance with
669 crystallographic data acquisition. We thank Diana Gimenez for preparation of the KLHL20
670 tracer used in FA KLHL20 competition assays. Some Figure elements were created with
671 BioRender (https:// BioRender.com/8n9fh89, https://BioRender.com/eg0oktl,
672 https://BioRender.com/l2psuaa).
673

674 **REFERENCES**

675 1 Li, K. & Crews, C. M. PROTACs: past, present and future. *Chem. Soc. Rev.*
676 **51**, 5214-5236 (2022). https://doi.org/10.1039/D2CS00193D
677 2 Zhao, L., Zhao, J., Zhong, K., Tong, A. & Jia, D. Targeted protein degradation:
678 mechanisms, strategies and application. *Sig. Transduct. Target. Ther.* **7**, 113
679 (2022). https://doi.org/10.1038/s41392-022-00966-4
680 3 Banik, S. M. *et al.* Lysosome-targeting chimaeras for degradation of
681 extracellular proteins. *Nature* **584**, 291-297 (2020).
682 https://doi.org/10.1038/s41586-020-2545-9

683 4 Korona, B. & Itzhaki, L. S. How to target membrane proteins for degradation:
684 Bringing GPCRs into the TPD fold. *J. Biol. Chem.* **300**, 107926 (2024).
685 https://doi.org/https://doi.org/10.1016/j.jbc.2024.107926
686 5 Zhong, G., Chang, X., Xie, W. & Zhou, X. Targeted protein degradation:
687 advances in drug discovery and clinical practice. *Sig. Transduct. Target. Ther.*
688 **9**, 308 (2024). https://doi.org/10.1038/s41392-024-02004-x
689 6 Konstantinidou, M. & Arkin, M. R. Molecular glues for protein-protein
690 interactions: Progressing toward a new dream. *Cell Chem. Biol.* **31**, 1064-
691 1088 (2024). https://doi.org/https://doi.org/10.1016/j.chembiol.2024.04.002
692 7 Sakamoto, K. M. *et al.* Protacs: Chimeric molecules that target proteins to the
693 Skp1–Cullin–F box complex for ubiquitination and degradation. *PNAS* **98**,
694 8554-8559 (2001). https://doi.org/doi:10.1073/pnas.141230798
695 8 Cardno, A., Kennedy, B. & Lindon, C. Cellular parameters shaping pathways
696 of targeted protein degradation. *Commun. Biol.* **8**, 691 (2025).
697 https://doi.org/10.1038/s42003-025-08104-w
698 9 He, Y. *et al.* DT2216—a Bcl-xL-specific degrader is highly active against Bcl-
699 xL-dependent T cell lymphomas. *J. Hematol. Oncol.* **13**, 95 (2020).
700 https://doi.org/10.1186/s13045-020-00928-9
701 10 Cao, C., He, M., Wang, L., He, Y. & Rao, Y. Chemistries of bifunctional
702 PROTAC degraders. *Chem. Soc. Rev.* **51**, 7066-7114 (2022).
703 https://doi.org/10.1039/D2CS00220E
704 11 Girardini, M., Maniaci, C., Hughes, S. J., Testa, A. & Ciulli, A. Cereblon versus
705 VHL: Hijacking E3 ligases against each other using PROTACs. *Biorg. Med.*
706 *Chem.* **27**, 2466-2479 (2019).
707 https://doi.org/https://doi.org/10.1016/j.bmc.2019.02.048
708 12 Hickey, C. M. *et al.* Co-opting the E3 ligase KLHDC2 for targeted protein
709 degradation by small molecules. *Nat. Struct. Mol. Biol.* **31**, 311-322 (2024).
710 https://doi.org/10.1038/s41594-023-01146-w
711 13 Deng, Z. *et al.* Harnessing the SPOP E3 Ubiquitin Ligase via a Bridged
712 Proteolysis Targeting Chimera (PROTAC) Strategy for Targeted Protein
713 Degradation. *J. Med. Chem.* **68**, 8634-8647 (2025).
714 https://doi.org/10.1021/acs.jmedchem.5c00295
715 14 Naito, M., Ohoka, N. & Shibata, N. SNIPERs—Hijacking IAP activity to induce
716 protein degradation. *Drug Discov. Today Technol.* **31**, 35-42 (2019).
717 https://doi.org/https://doi.org/10.1016/j.ddtec.2018.12.002
718 15 Békés, M., Langley, D. R. & Crews, C. M. PROTAC targeted protein
719 degraders: the past is prologue. *Nat. Rev. Drug Discov.* **21**, 181-200 (2022).
720 https://doi.org/10.1038/s41573-021-00371-6
721 16 Dai, M.-Y. *et al.* High-potency PD-1/PD-L1 degradation induced by Peptide-
722 PROTAC in human cancer cells. *Cell Death Dis.* **13**, 924 (2022).
723 https://doi.org/10.1038/s41419-022-05375-7
724 17 Farrell, B. M., Gerth, F., Yang, C.-H. R. & Yeh, J. T.-H. A synthetic KLHL20
725 ligand to validate CUL3KLHL20 as a potent E3 ligase for targeted protein
726 degradation. *Genes Dev.* (2022). https://doi.org/10.1101/gad.349717.122
727 18 Lim, S. *et al.* bioPROTACs as versatile modulators of intracellular therapeutic
728 targets including proliferating cell nuclear antigen (PCNA). *PNAS* **117**, 5791-
729 5800 (2020). https://doi.org/doi:10.1073/pnas.1920251117
730 19 Kortemme, T. De novo protein design; From new structures to programmable
731 functions. *Cell* **187**, 526-544 (2024). https://doi.org/10.1016/j.cell.2023.12.028

20 Ovchinnikov, S. & Huang, P.-S. Structure-based protein design with deep learning. *Curr. Opin. Chem. Biol.* **65**, 136-144 (2021). https://doi.org/https://doi.org/10.1016/j.cbpa.2021.08.004

21 Albanese, K. I., Barbe, S., Tagami, S., Woolfson, D. N. & Schiex, T. Computational protein design. *Nat. Rev. Methods Primers* **5**, 13 (2025). https://doi.org/10.1038/s43586-025-00383-1

22 Fox, D. R., Taveneau, C., Clement, J., Grinter, R. & Knott, G. J. Code to complex: AI-driven de novo binder design. *Structure* (2025). https://doi.org/10.1016/j.str.2025.08.007

23 Jumper, J. *et al.* Highly accurate protein structure prediction with AlphaFold. *Nature* **596**, 583-589 (2021). https://doi.org/10.1038/s41586-021-03819-2

24 Niazi, S. K. Critical assessment of AI-based protein structure prediction: Fundamental challenges and future directions in drug discovery. *CSB Reports* **2**, 100064 (2025). https://doi.org/https://doi.org/10.1016/j.csbr.2025.100064

25 Watson, J. L. *et al.* De novo design of protein structure and function with RFdiffusion. *Nature* **620**, 1089-1100 (2023). https://doi.org/10.1038/s41586-023-06415-8

26 Dauparas, J. *et al.* Robust deep learning–based protein sequence design using ProteinMPNN. *Science* **378**, 49-56 (2022). https://doi.org/10.1126/science.add2187

27 Bennett, N. R. *et al.* Improving de novo protein binder design with deep learning. *Nat. Comm.* **14**, 2625 (2023). https://doi.org/10.1038/s41467-023-38328-5

28 Cao, L. *et al.* Design of protein-binding proteins from the target structure alone. *Nature* **605**, 551-560 (2022). https://doi.org/10.1038/s41586-022-04654-9

29 Pacesa, M. *et al.* One-shot design of functional protein binders with BindCraft. *Nature* (2025). https://doi.org/10.1038/s41586-025-09429-6

30 Kim, S., Park, H.-S. & Oh, B.-H. Computational design of an apoptogenic protein that binds BCL-xL and MCL-1 simultaneously and potently. *CSBJ* **20**, 3019-3029 (2022). https://doi.org/10.1016/j.csbj.2022.06.021

31 Castro, K. M. *et al.* Accurate single-domain scaffolding of three nonoverlapping protein epitopes using deep learning. *Nat. Chem. Biol.* (2025). https://doi.org/10.1038/s41589-025-02083-z

32 Huang, B. *et al.* Designed endocytosis-inducing proteins degrade targets and amplify signals. *Nature* **638**, 796-804 (2025). https://doi.org/10.1038/s41586-024-07948-2

33 Suiter, C. C. *et al.* Multiplex design and discovery of proximity handles for programmable proteome editing. *bioRxiv*, 2025.2010.2013.681693 (2025). https://doi.org/10.1101/2025.10.13.681693

34 Vogler, M. *et al.* The BCL2 family: from apoptosis mechanisms to new advances in targeted therapy. *Sig. Transduct. Target. Ther.* **10**, 91 (2025). https://doi.org/10.1038/s41392-025-02176-0

35 Czabotar, P. E. & Garcia-Saez, A. J. Mechanisms of BCL-2 family proteins in mitochondrial apoptosis. *Nat. Rev. Mol. Cell Biol.* **24**, 732-748 (2023). https://doi.org/10.1038/s41580-023-00629-4

36 Kvansakul, M. & Hinds, M. G. The Bcl-2 family: structures, interactions and targets for drug discovery. *Apoptosis* **20**, 136-150 (2015). https://doi.org/10.1007/s10495-014-1051-7

37 Jenson, J. M. *et al.* Peptide design by optimization on a data-parameterized protein interaction landscape. *PNAS* **115**, E10342-E10351 (2018). https://doi.org/10.1073/pnas.1812939115

38 Procko, E. *et al.* A Computationally Designed Inhibitor of an Epstein-Barr Viral Bcl-2 Protein Induces Apoptosis in Infected Cells. *Cell* **157**, 1644-1656 (2014). https://doi.org/10.1016/j.cell.2014.04.034

39 Pannecoucke, E. *et al.* Cell-penetrating Alphabody protein scaffolds for intracellular drug targeting. *Sci. Adv.* **7**, eabe1682 (2021). https://doi.org/doi:10.1126/sciadv.abe1682

40 Osterlund, E. J. *et al.* Efficacy and specificity of inhibitors of BCL-2 family protein interactions assessed by affinity measurements in live cells. *Sci. Adv.* **8**, eabm7375 (2022). https://doi.org/doi:10.1126/sciadv.abm7375

41 Bricelj, A. *et al.* Design, Synthesis, and Evaluation of BCL-2 Targeting PROTACs. *Chem. Eur. J.* **30**, e202400430 (2024). https://doi.org/https://doi.org/10.1002/chem.202400430

42 Khan, S. *et al.* A selective BCL-XL PROTAC degrader achieves safe and potent antitumor activity. *Nat. Med.* **25**, 1938-1947 (2019). https://doi.org/10.1038/s41591-019-0668-z

43 Chen, Z., Picaud, S., Filippakopoulos, P., D'Angiolella, V. & Bullock, A. N. Structural Basis for Recruitment of DAPK1 to the KLHL20 E3 Ligase. *Structure* **27**, 1395-1404.e1394 (2019). https://doi.org/10.1016/j.str.2019.06.005

44 Albanese, K. I. *et al.* Rationally seeded computational protein design of a-helical barrels. *Nat. Chem. Biol.* **20**, 991-999 (2024). https://doi.org/10.1038/s41589-024-01642-0

45 Rhys, G. G. *et al.* De novo designed peptides for cellular delivery and subcellular localisation. *Nat. Chem. Biol.* **18**, 999-1004 (2022). https://doi.org/10.1038/s41589-022-01076-6

46 Zhou, J. & Grigoryan, G. Rapid search for tertiary fragments reveals protein sequence–structure relationships. *Protein Sci.* **24**, 508-524 (2015). https://doi.org/https://doi.org/10.1002/pro.2610

47 Huang, P.-S. *et al.* RosettaRemodel: A Generalized Framework for Flexible Backbone Protein Design. *PLoS One* **6**, e24109 (2011). https://doi.org/10.1371/journal.pone.0024109

48 Fletcher, J. M. *et al.* De novo coiled-coil peptides as scaffolds for disrupting protein–protein interactions. *Chem. Sci.* **9**, 7656-7665 (2018). https://doi.org/10.1039/C8SC02643B

49 Acevedo-Jake, A. M. *et al.* Grafted Coiled-Coil Peptides as Multivalent Scaffolds for Protein Recognition. *ACS Chem. Biol.* **20**, 1309-1318 (2025). https://doi.org/10.1021/acschembio.5c00137

50 Lawrence, M. C. & Colman, P. M. Shape Complementarity at Protein/Protein Interfaces. *J. Mol. Biol.* **234**, 946-950 (1993). https://doi.org/https://doi.org/10.1006/jmbi.1993.1648

51 Alford, R. F. *et al.* The Rosetta All-Atom Energy Function for Macromolecular Modeling and Design. *J. Chem. Theory Comput.* **13**, 3031-3048 (2017). https://doi.org/10.1021/acs.jctc.7b00125

52 Bolomsky, A. *et al.* MCL-1 inhibitors, fast-lane development of a new class of anti-cancer agents. *J. Hematol. Oncol.* **13**, 173 (2020). https://doi.org/10.1186/s13045-020-01007-9

53 Vermes, I., Haanen, C., Steffens-Nakken, H. & Reutellingsperger, C. A novel assay for apoptosis Flow cytometric detection of phosphatidylserine expression on early apoptotic cells using fluorescein labelled Annexin V. *J. Immunol. Methods* **184**, 39-51 (1995). https://doi.org/https://doi.org/10.1016/0022-1759(95)00072-I

54 Li, Z. *et al.* De novo designed protein guiding targeted protein degradation. *Nat. Comm.* **16**, 6598 (2025). https://doi.org/10.1038/s41467-025-62050-z

55 Ma, B. *et al.* A Top-Down Design Approach for Generating a Peptide PROTAC Drug Targeting Androgen Receptor for Androgenetic Alopecia Therapy. *J. Med. Chem.* **67**, 10336-10349 (2024). https://doi.org/10.1021/acs.jmedchem.4c00828

56 Ongkingco, J. F., Hong, S. H., Toth, E. D., Nguyen, T. & Arora, P. S. Reengineering of a Proteomimetic Pan-Ras Inhibitor into a Ras Degrader. *Angew. Chem. Int. Ed.* **64**, e202507092 (2025). https://doi.org/https://doi.org/10.1002/anie.202507092

57 Hong, S. H., Nguyen, T., Ongkingco, J. F., Nazzaro, A. & Arora, P. S. From Concepts to Inhibitors: A Blueprint for Targeting Protein–Protein Interactions. *Chem. Rev.* **125**, 6819-6869 (2025). https://doi.org/10.1021/acs.chemrev.5c00046

58 Cotet, T.-S. *et al.* Crowdsourced Protein Design: Lessons From the Adaptyv EGFR Binder Competition. *bioRxiv*, 2025.2004.2017.648362 (2025). https://doi.org/10.1101/2025.04.17.648362

59 Overath, M. D. *et al.* Predicting Experimental Success in De Novo Binder Design: A Meta-Analysis of 3,766 Experimentally Characterised Binders. *bioRxiv*, 2025.2008.2014.670059 (2025). https://doi.org/10.1101/2025.08.14.670059

60 Vosbein, P., Paredes Vergara, P., Huang, D. T. & Thomson, A. R. AlphaFold Ensemble Competition Screens Enable Peptide Binder Design with Single-Residue Sensitivity. *ACS Chem. Biol.* **19**, 2198-2205 (2024). https://doi.org/10.1021/acschembio.4c00418

61 Zhao, H., Piszczek, G. & Schuck, P. SEDPHAT – A platform for global ITC analysis and global multi-method analysis of molecular interactions. *Methods* **76**, 137-148 (2015). https://doi.org/https://doi.org/10.1016/j.ymeth.2014.11.012

62 Scheuermann, T. H. & Brautigam, C. A. High-precision, automated integration of multiple isothermal titration calorimetric thermograms: New features of NITPIC. *Methods* **76**, 87-98 (2015). https://doi.org/https://doi.org/10.1016/j.ymeth.2014.11.024

63 Kabsch, W. XDS. *Acta Crystallogr. Sect. D.* **66**, 125-132 (2010). https://doi.org/doi:10.1107/S0907444909047337

64 Winter, G. *et al.* DIALS: implementation and evaluation of a new integration package. *Acta Crystallogr. Sect. D.* **74**, 85-97 (2018). https://doi.org/doi:10.1107/S2059798317017235

65 Evans, P. R. & Murshudov, G. N. How good are my data and what is the resolution? *Acta Crystallogr. Sect. D.* **69**, 1204-1214 (2013). https://doi.org/doi:10.1107/S0907444913000061

66 McCoy, A. J. *et al.* Phaser crystallographic software. *J. Appl. Crystallogr.* **40**, 658-674 (2007). https://doi.org/doi:10.1107/S0021889807021206

67 Adams, P. D. *et al.* PHENIX: building new software for automated crystallographic structure determination. *Acta Crystallogr. Sect. D.* **58**, 1948-1954 (2002). https://doi.org/doi:10.1107/S0907444902016657

880